https://doi.org/10.1016/j.est.2021.103027

Enhancement of lithium-ion battery thermal management with the divergent-shaped channel cold plate

Wei Kong[1], Kejun Zhu[1], Xipo Lu[1], Jingtao Jin[1], Meng Ni[2]**

[1] School of Energy and Power, Jiangsu University of Science and Technology, 212003, Zhenjiang, Jiangsu, China; wkong@just.edu.cn

[2] Building Energy Research Group, Department of Building and Real Estate, The Hong Kong Polytechnic University, Hung Hom, Kowloon, Hong Kong, China; meng.ni@ployu.edu.hk

* Corresponding authors.

Abstract

Effective thermal management is critical to the performance and durability of lithium ion batteries for electric vehicles. Unlike conventional cold plate with straight channels, a new cold plate with divergent-shaped channels is proposed and evaluated to minimize the maximum temperature and the pressure drop of the cold plate. Compared with the conventional straight-shaped channels, the divergent-shaped channels exhibit high performance with a higher heat dissipation capacity and a lower frictional resistance. In order to further reduce the local flow resistance, the divergent-shaped channels with 2 inlets and 1 outlet are developed and evaluated. It is found that the new design with 2 inlets and 1 outlet can successfully decrease the pressure drop by 7.2% and decrease the maximum temperature difference from 4.69 K to 3.94 K. Finally, battery cooling modules with the counter flow configuration are constructed, which achieves the smaller maximum temperature difference. This research contributes to the development of effective and efficient battery cooling systems for electric vehicles.

Keywords: Battery thermal management (BTM), liquid cooling, cold plate, divergent-shaped channel

Highlights

- A divergent-shaped channel cold plate is proposed to enhance the BTM performance.
- A cold plate with 2 inlets and 1 outlet is developed to reduce the local resistance.
- A battery cooling module with the counter flow are constructed for BTM.

Introduction

Recently, there has been a surge of interest in the lithium-ion (Li-ion) battery as the power source of electric vehicles due to its advantages of high specific energy density, long lifespan, low self-discharge rate, high voltage platform, and no memory effect [1-4]. During the discharging process of Li-ion battery, enormous heat is generated from the electrochemical reaction and various overpotential losses. This heat generation could significantly increase the battery temperature, which can decrease the battery performance and even cause fire or explosion [5-7]. Therefore, the battery thermal management system (BTMS) is a crucial component of electric vehicles to maintain the Li-ion battery in the suitable operating temperature range and avoid the negative impact of temperature [8-12].

The liquid cooled BTMS has been proven to be one of the most efficient BTMSs and more commercially mature [13-15]. In the liquid cooled BTMS, the cold plate is commonly employed between the cells owing to its high heat exchange efficiency. The heat generated during the battery discharge process is removed by the coolant flowing in the cold plate. Recently considerable literature has grown up on the performance of cold plates [16-19]. Jarrett et al. optimized the cold plate with serpentine-shaped channel. The results show that compared with the reference design, the average temperature of the optimized design can be decreased by about 14% [20]. Deng et al established a numerical model of the serpentine-shaped channel cold plate and compared different layouts of channels. It is found that the layout of channels with the flowing along the length-direction has a better cooling performance [21]. Su et al. developed a serpentine-shaped channel cold plate with two inlets and outlets [22]. However, for the serpentine-shaped channel cold plate, the pressure drop is usually higher than that of the straight-shaped channel cold plate due to the longer channel length, resulting in the more energy consumption.

Many scholars are trying to explore the cooling behavior of the straight-shaped channel cold plate [18]. Zhu et al. adopted the orthogonal experimental design method to reduce the temperature of the straight-shaped channel cold plate and obtained the optimal case satisfying the various requirements of BTMS [23]. Huo et al. investigated the effect of channel number on the thermal behavior of the straight-shaped channel cold plate, finding that increasing the number of channels can decrease the battery maximum temperature [24]. Qian et al. reported that the pressure drop is sensitive to the channel

width. The pressure drop can be reduced by 55% as the channel width is changed from 3 mm to 6 mm [25]. The wedge-shaped channel cold plate was designed by Rao et al. to improve the heat exchange efficiency of the straight-shaped channel cold plate [26]. For the wedge-shaped channel, the inlet area of channel is the same as the outlet area of channel, but the aspect ratio of outlet is smaller than that of inlet. It is found that the maximum temperature of the cold plate decreases but the pressure drop increases with decreasing outlet aspect ratio. In order to further reduce the flow resistance in the straight-shaped channel cold plate, a streamline-shaped channel cold plate was proposed by Huang et al [27]. The results reveal that the use of streamline channel design can decrease flow resistance generated near the sharp corner but has negligible effect on the maximum temperature.

Although the wedge-shaped channel cold plate or the streamline-shaped channel cold plate can reduce either maximum temperature or pressure drop, they cannot simultaneously minimize the maximum temperature and the pressure drop. Reducing the maximum temperature and the pressure drop are both important for the effective and efficient cooling of batteries for electric vehicles. Therefore, in this work, the divergent-shaped channel is proposed and demonstrated to be effective in enhancing the heat dissipation capacity and reducing the pressure drop simultaneously. Subsequently, the divergent-shaped channel cold plate with two inlets is designed to further reduce the local flow resistance. Finally, on the basis of the above cold plate design, a battery cooling module with the counter flow configuration is constructed.

2. Modeling

2.1. Physical model

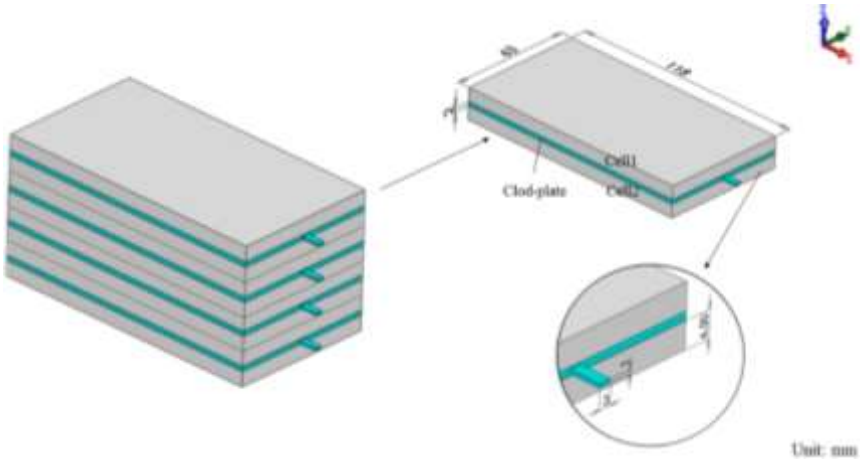

Fig. 1. Schematic of the model structure

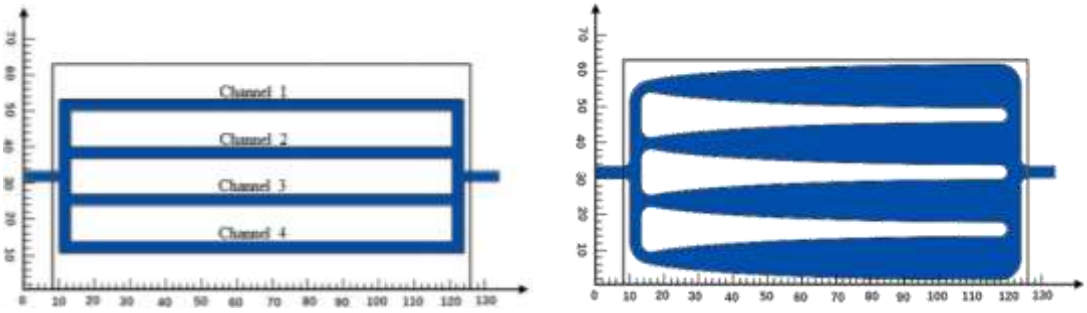

(a) (b)

Fig. 2. The cold plate with (a) the straight-shaped channel (b) the divergent-shaped channel

The enormous number of batteries are used in electric vehicles to meet the requirement of power and energy. In such a battery pack, the behaviors of each repeating unit are almost identical. Therefore, in the present study, a repeating unit is selected as the computational domain, which consists of two batteries and one cold plate, as shown in Fig. 1. Moreover, the size of the batteries and cold plate is also given in Fig. 1. Two 3D models were developed for the cold plates, as illustrated in Fig. 2. The material of cold plate is aluminum and the coolant in cold plate is liquid water. Table 1 provides the physical properties of water, cold plate, and battery.

Table 1 Property parameters

	ρ (kg m^{-3})	C_p (J kg^{-1} K^{-1})	k (W m^{-1} K^{-1})	v_w (kg m^{-1} s^{-1})
Water	998.2	4182	0.6	0.001003
Cold plate	2719	871	202.4	--
Battery	2450	1108	3.9	--

2.2. Governing equations and boundaries

The Reynolds number is calculated based on inlet velocity and geometry size of channel, which is smaller than 2300. Thus, the fluid flow is laminar and the corresponding momentum equation below is used to describe the coolant flow.

$$\frac{\partial \vec{v}}{\partial t}+\left(\vec{v}\cdot\nabla\right)\vec{v}=-\frac{\nabla P}{\rho_{\mathrm{w}}}+\frac{\mu}{\rho_{\mathrm{w}}}\nabla^2\vec{v} \tag{1}$$

The mass and energy conservation equations of coolant can be written as

$$\frac{\partial \rho_w}{\partial t}+\nabla\cdot(\rho_w\vec{v})=0 \tag{2}$$

$$\frac{\partial}{\partial t}(\rho_w C_{pw}T_w)+\nabla\cdot(-k_w\nabla T_w+\rho_w C_{pw}T_w\vec{v})=0 \tag{3}$$

The energy conservation equations of cold plate and battery can be expressed as Eq. 4

and 5, respectively.

$$\frac{\partial}{\partial t}(\rho_c C_{pc} T_c) + \nabla \cdot (-k_c \nabla T_c) = 0 \tag{4}$$

$$\frac{\partial}{\partial t}(\rho_b C_{pb} T_b) + \nabla \cdot (-k_b \nabla T_b) = Q \tag{5}$$

In the above equations, the subscripts "w", "c" and "b" denote the water, cold plate and battery, respectively. ρ, T, C_p and k are the density, temperature, specific heat capacity and thermal conductivity, respectively. $\vec{v}$ and P are the velocity and pressure, respectively. Q is the heat source of battery.

The setting of boundaries and initial conditions are necessary to solve the above coupled governing equations. The initial temperature of model is specified as the ambient temperature 298 K. For the inlet, the mass flow rate is set at 2 g/s, and inlet temperature is set at 298 K. For the outlet, the gauge pressure is set at 0 Pa. The heat generation of battery Q is set at 240000 Wm^{-3}, which corresponds to the 5C discharge, as reported by Rao et al[25].

2.3. Model validation

The ANSYS FLUENT was employed to build the model and solve the governing equations presented in the previous section. Grid independence check was conducted by implementing the simulations with different grid numbers, as shown in Table 2. Fig. 3 displays the impact of grid number on the pressure drop and temperature difference. It is obvious that the difference between Grid 5 and Grid 6 is negligible. Thus, the grid number of Grid 5 is sufficient and used in the subsequent simulations. To verify the accuracy of the numerical results, a battery model without the cold plate is built based on the parameters given in Ref. [25]. The maximum temperature (T_{max}) of battery is consistent with the data reported in Ref. [25], which validates the numerical method in this work.

Table 2 Six models with different grid number

Type	Grid 1	Grid 2	Grid 3	Grid 4	Grid 5	Grid 6
Grid number	1549464	2199476	3001518	4717150	5314225	6434905

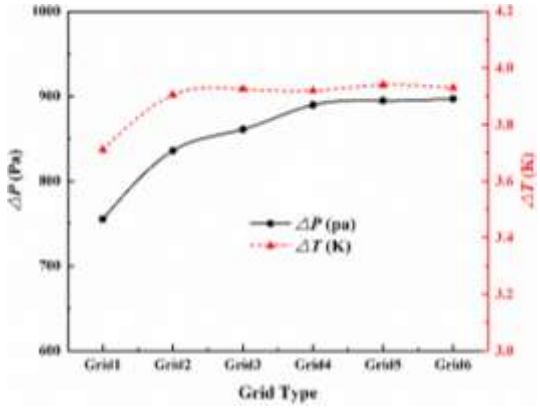

Fig. 3. Effects of grid number

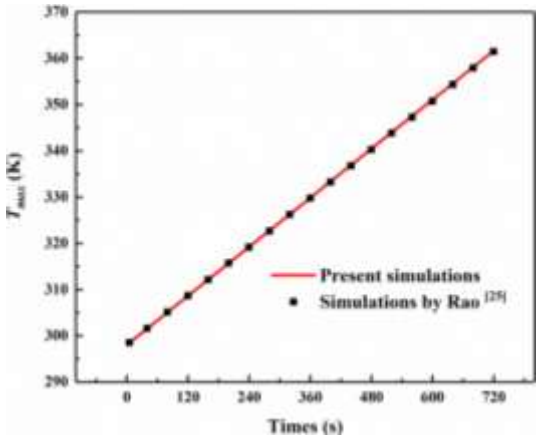

Fig. 4. Comparison of the numerical results and the data in Ref. [25]

3. Results and discussion

3.1. The distribution of temperature

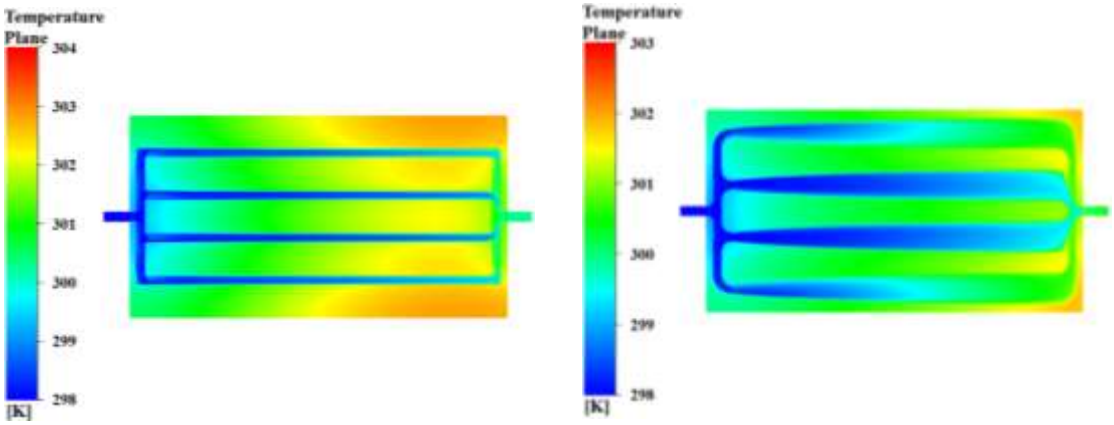

（a） （b）

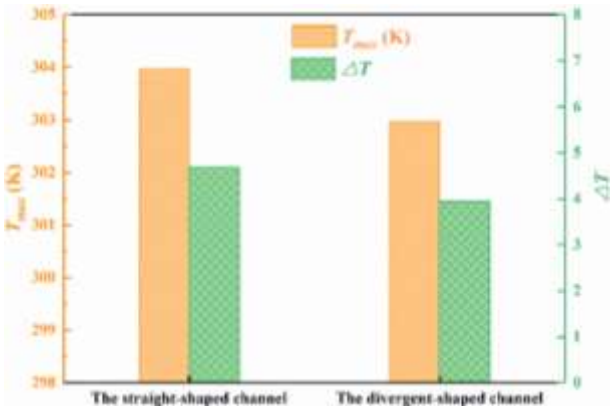

（c）

Fig. 5. The temperature distribution at the mid-profile of plates (a) the straight-shaped channel (b) the divergent-shaped channel (c) the maximum temperature and temperature difference

Fig. 5 compares the temperature distribution for the two designs. The maximum temperature occurs near the two corners of the outlet side both designs. The reason is that the coolant temperature rises along the flow direction, resulting in the decrease of heat dissipation capacity in the flow direction. Meanwhile, the long distance between the corner and side channel hinders the heat transfer. In addition, for the divergent-shaped channel, the maximum temperature is 302.96 K, which is 1 K lower than that of the straight-shaped channel, as shown in Fig. 5c. Compared with the straight-shaped channel, the increasing cross section area along flow direction promotes the heat dissipation of downstream region for the divergent-shaped channel. On the other hand, the distance between the corner and side channel is shortened, leading to the reduction of the thermal resistance.

3.2. The distribution of pressure

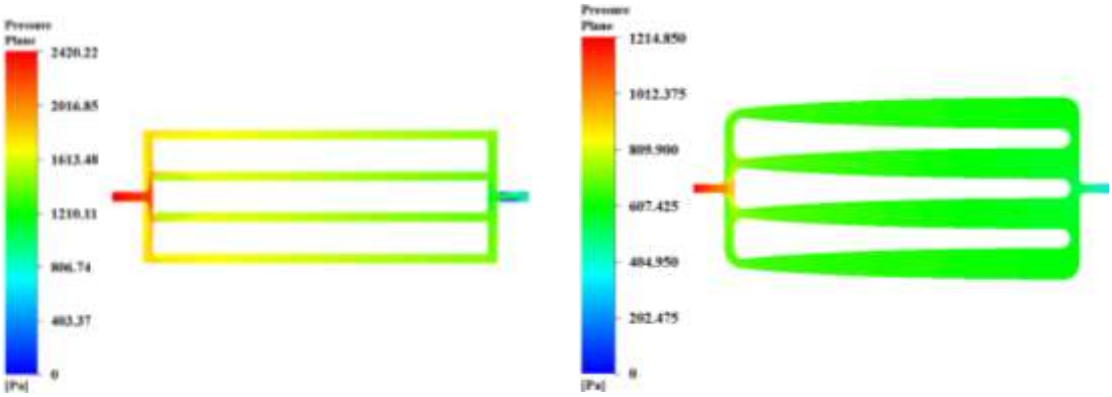

(a) (b)

Fig. 6. The pressure distribution (a) the straight-shaped channel (b) the divergent-

shaped channel

Fig. 6 compares the pressure distribution of the straight-shaped channel with the divergent-shaped channel. The pressure drop of the divergent-shaped channel is only 1214.9 Pa, 49.8% lower than that of the straight-shaped channel (2420.2 Pa). Obviously, the design of the divergent-shaped channel is beneficial for reducing the pressure drop and external energy consumption. The frictional resistance is a major factor causing pressure loss, which is proportional to the velocity. For the divergent-shaped channel, the velocity decreases along the flow direction due to the increasing cross-sectional area, resulting in the lower frictional resistance. This finding is further verified by the distribution of pressure drop in the four branch channels, which are numbered as channel 1 to channel 4 as displayed in Fig. 2. As shown in Fig. 7, the maximum pressure drop in branch channel is 129.46 Pa for the divergent-shaped channel, which is only 40% of the minimum pressure drop in branch channel for the straight-shaped channel.

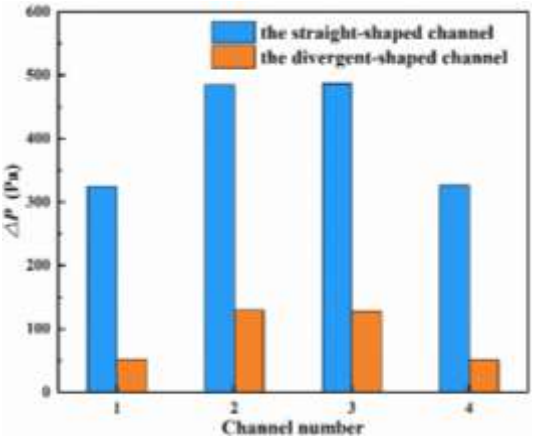

Fig. 7. The pressure drop in four channels

3.3 The effect of inlet area

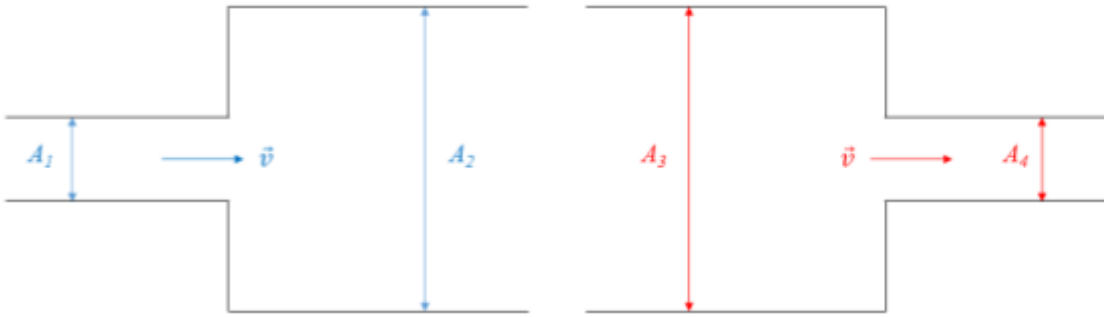

(a) (b)

Fig.8. the schematic of (a) the divergent-shaped channel (b) the convergent-shaped channel

The local resistance is another crucial factor causing pressure loss, which is strongly dependent on the change of channel cross section area. For the divergent-shaped channel, as plotted in Fig. 8a, the pressure loss caused by the local resistance can be written as

$$\Delta p_{local}^{d} = (1- \frac{A_1}{A_2})^2 \frac{\rho}{2} \vec{v}^2 \quad (6)$$

For the convergent-shaped channel, as plotted in Fig. 8b, the pressure loss caused by the local resistance can be expressed as

$$\Delta p_{local}^{c} = \frac{1}{2}(1- \frac{A_4}{A_3}) \frac{\rho}{2} \vec{v}^2 \quad (7)$$

Where Δp_{local} is the pressure loss caused by the local resistance, the superscripts "*d*" and "*c*" denote the divergent-shaped channel and the convergent-shaped channel, respectively. *A* is the cross-section area of channel, the superscripts "*1*", "*2*", "*3*" and "*4*" denote different positions as illustrated in Fig. 8.

It is as expected that the inlet and outlet area are closely related to the local resistance. The influence of inlet area was investigated with the assumption that the inlet area is the same as outlet area. The mass flow rate is set as constant at 2.5 g s^{-1}. Fig. 9a presents the relationship between the pressure drop and inlet area. The pressure loss falls sharply with the increasing inlet area. When the inlet area rises from 3 mm^2 to 6 mm^2, the pressure loss declines from 894.81 Pa to 459.16 Pa, which is decreased by about 48.7%. However, the maximum temperature (T_{max}) and temperature difference (ΔT) are almost independent on the inlet area, as shown in Fig. 9b.

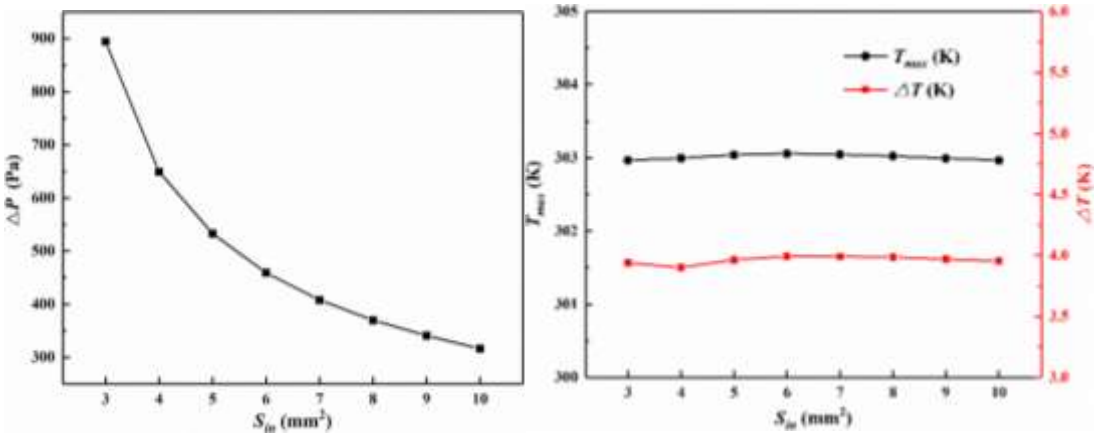

(a) (b)

Fig. 9. The effect of inlet area (a) the pressure drop (b) the temperature

Although the pressure loss is lower with a larger inlet area, increasing inlet or outlet area will increase the probability of coolant leakage. Therefore, it is meaningful to optimize the inlet area when the sum of inlet and outlet area (S_{tot}) is fixed. As displayed in Fig. 10, as inlet area increases, the pressure loss decreases first and then increases for

different S_{tot}, indicating the optimal inlet area with the lowest pressure loss. The minimal pressure drops for S_{tot} of 14 mm^2, 16 mm^2 and 18 mm^2 are 402.72 Pa, 365.71 Pa and 336.34 Pa, respectively, corresponding to the optimal inlet areas of 8.1 mm^2, 9.3 mm^2 and 10.4 mm^2, respectively. Clearly, the optimal inlet area (S_{in}) is proportional to the S_{tot}. Fig. 11 shows the relationship between S_{in} *and* S_{tot}. It is obvious that the optimal S_{in} is dependent approximately linearly on S_{tot}, which can be formulized as:

$$S_{in} = -0.078 + 0.584 \times S_{tot} \tag{8}$$

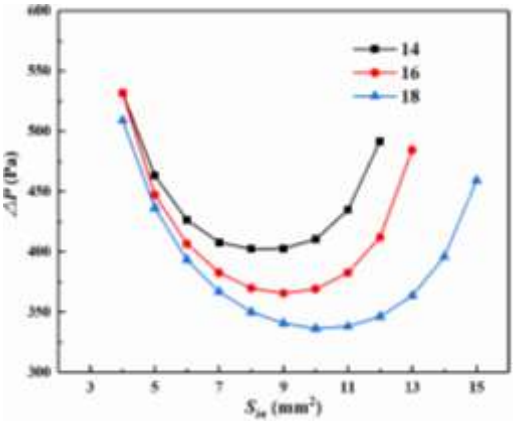

Fig. 10. The effect of inlet area on the pressure drop

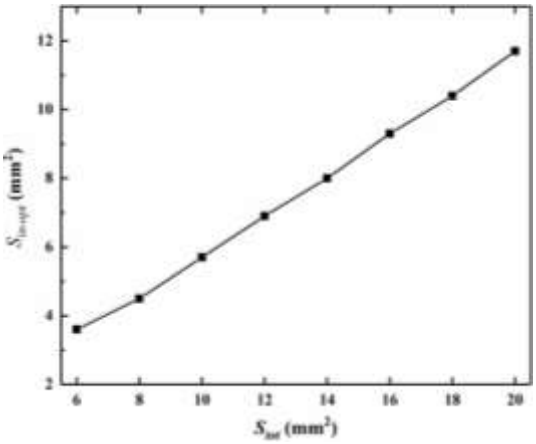

Fig. 11. The dependence of S_{in} on S_{tot}

3.4 The effect of manifold

In order to further reduce the local resistance, the cold plate with 2 inlets and 1 outlet was proposed on the basis of the divergent-shaped channel. The S_{tot} is 12 mm^2, and the two inlet areas are the same, which is 3.45 mm^2 calculated by Eq. 8. As can be seen from Fig. 12, compared with the cold plate with 1 inlet and 1 outlet, the cold plate with 2 inlets and 1 outlet can decrease the pressure loss to 419.7 Pa, which is decreased by 7.2%. The maximum temperature difference decreases from 4.69 K to 3.94 K. The decrease of pressure drop can be explained by the Eq. 6. The improvement of cooling

performance is attributed to the more uniform mass flow distribution. The mass flow rate in channel 1(4) increases from 0.37 g s^{-1} to 0.54 g s^{-1}, as illustrated in Fig. 13.

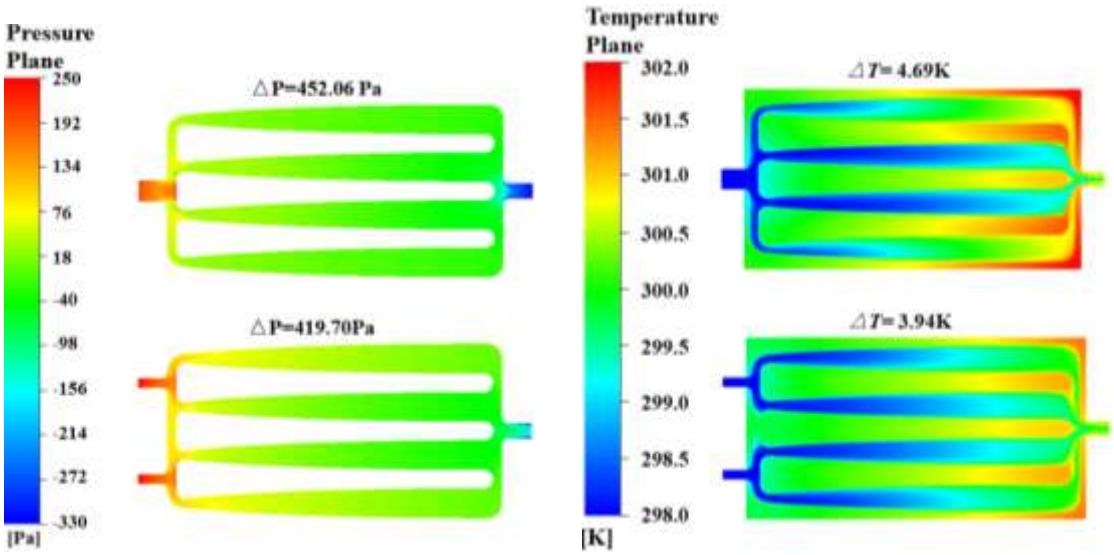

Fig. 12. The comparison of (a) pressure distribution and (b) temperature distribution at the mid-profile of cold plates

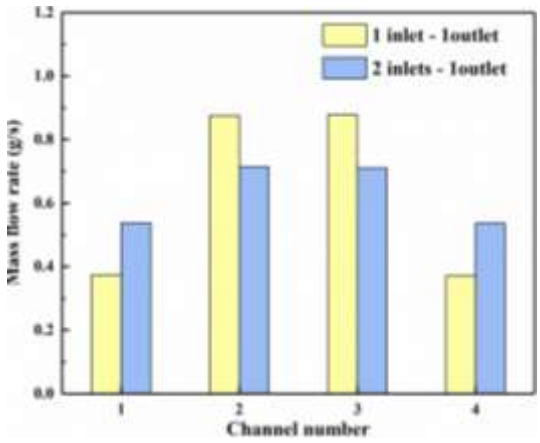

Fig. 13. The mass flow rate in different channels

3.5 The battery cooling module

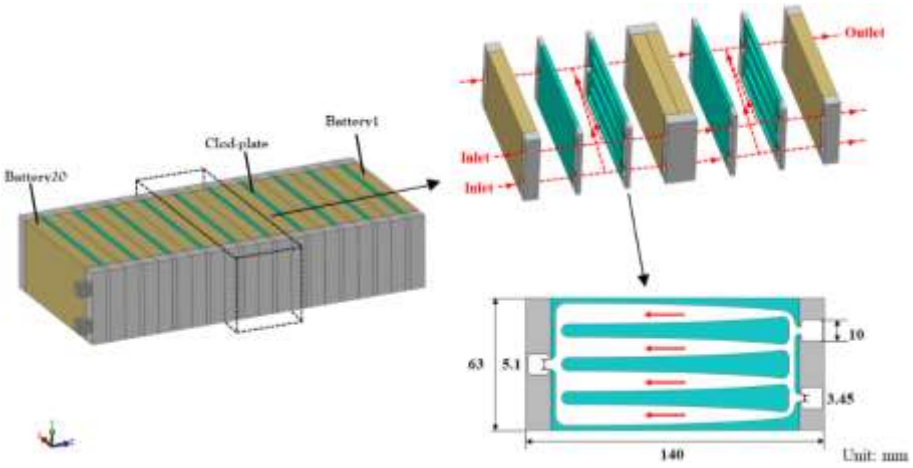

（a）

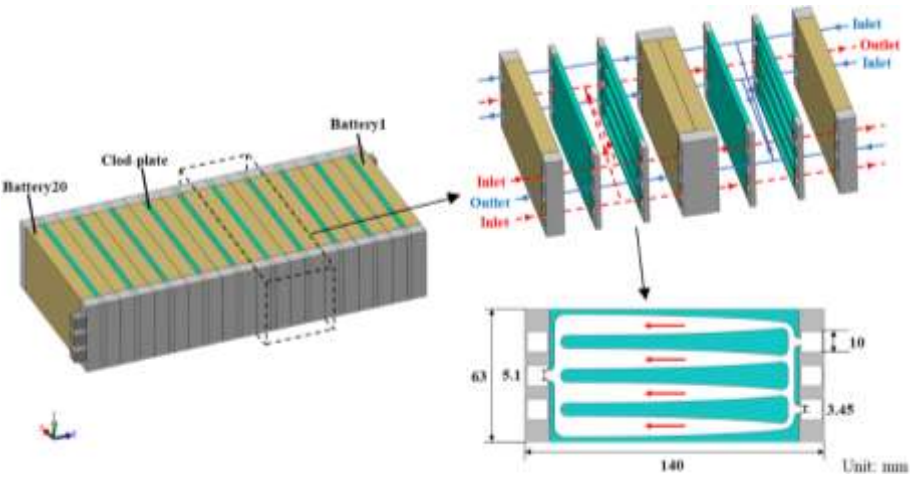

（b）

Fig. 14. Schematic of (a) the parallel flow and (b) the counter flow structure

In this section, the battery cooling modules with the parallel flow and counter flow are constructed. In adjacent cold plates, the flow direction of coolant is the same as parallel flow, and the opposite is counter flow, as shown in Fig. 14. The total mass flow is 25 g s^{-1}. Fig. 15 displays the temperature distribution at the mid-profile of batteries for the two designs. For the parallel flow, the high temperature occurs at regions near the outlets of cold plate due to the same flow direction of coolant. However, for the counter flow, the high temperature appears at the middle of the batteries because of the different flow directions of coolant. Although the temperature distribution characteristics are completely different for the two designs, the maximum temperature is almost the same, as can been seen in Fig. 16. Moreover, the average maximum temperature difference of the counter flow is 2.72 K, 21.2 % lower than that of the parallel flow (3.45 K).

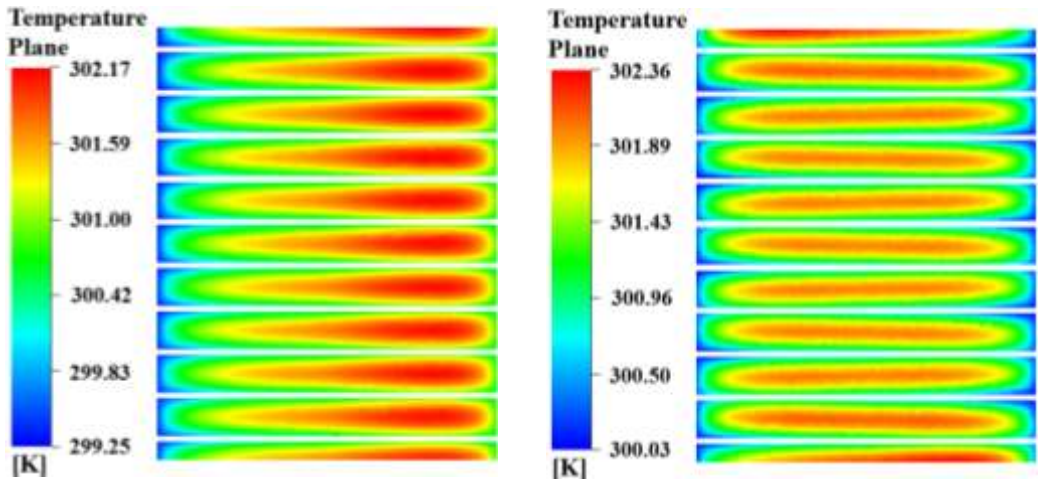

（a） （b）

Fig. 15. The temperature distribution at the mid-profile of batteries (a) the parallel flow (b) counter flow and (c) the comparison of maximum temperature and temperature difference

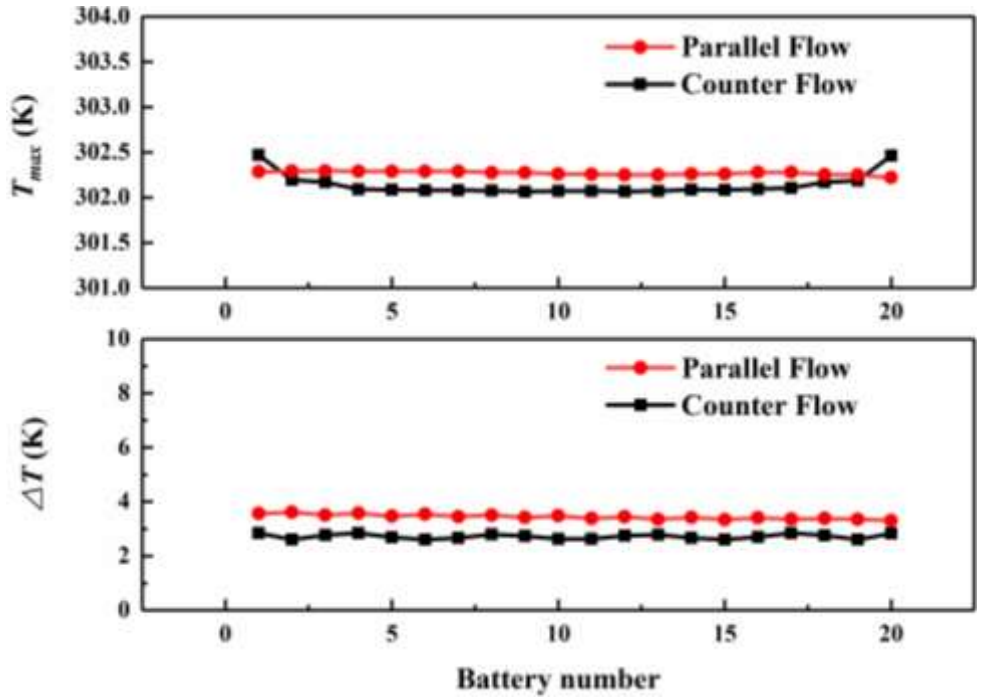

Fig. 16. The comparison of maximum temperature and temperature difference

4. Summary and conclusions

In this work, the divergent-shaped channel is proposed to enhance the heat dissipation capacity and reduce the frictional resistance. In order to further decrease the local resistance, the divergent-shaped channel cold plate with two inlets is designed. Finally, on the basis of the above cold plate design, the battery cooling modules with the parallel flow and counter flow are constructed. The conclusions are listed as follows.

(1) Compared with the straight-shaped channel, the increasing cross-sectional area along flow direction promotes the heat dissipation of downstream region for the divergent-shaped channel. Moreover, for the divergent-shaped channel, the velocity decreases along the flow direction due to the increasing cross-sectional area, resulting in the lower frictional resistance.

(2) The pressure loss falls sharply with the increase of inlet area. However, the maximum temperature (T_{max}) and temperature difference (ΔT) are almost independent on the inlet area.

(3) When the cold plate with 2 inlets and 1 outlet was adopted on the basis of the divergent-shaped channel, the pressure drop is decreased by 7.2% and the maximum temperature difference decreases from 4.69 K to 3.94 K.

(4) The battery cooling module with the parallel flow and counter flow are constructed. Although the temperature distribution characteristics are completely different for the two designs, the maximum temperature is almost the same. In addition, the average maximum temperature difference of the counter flow is 2.72 K, 21.2 % lower than that of the parallel flow of 3.45 K.

Acknowledgments We gratefully acknowledge the financial support of Zhenjiang Key Laboratory of Marine Power Equipment Performance(SS2018006), the National Science Foundation of China (21701083). M. Ni thanks the funding support from The Hong Kong Polytechnic University (G-YW2D) and grants (Project Number: PolyU 152214/17E and PolyU 152064/18E) from Research Grant Council, University Grants Committee, Hong Kong SAR.

References

[1] Chen Y, Wang Y, Shen X, Cai R, Yang H, Xu K, Yuan A, Ji Z. Cyanide-metal framework derived CoMoO4/Co3O4 hollow porous octahedrons as advanced anodes for high performance lithium ion batteries. J Mater Chem A Mater. 2018;6:1048-56.

[2] Yang H, Xie Y, Zhu M, Liu Y, Wang Z, Xu M, Lin S. Hierarchical porous MnCo2O4 yolk-shell microspheres from MOFs as secondary nanomaterials for high power lithium ion batteries. Dalton Trans. 2019;48:9205-13.

[3] Wu B, Xie Y, Meng Y, Qian C, Chen Y, Yuan A, Guo X, Yang H, Wan S, Lin S. Construction of unique heterogeneous cobalt–manganese oxide porous microspheres for the assembly of long-cycle and high-rate lithium ion battery anodes. J Mater Chem A Mater. 2019;7:6149-60.

[4] Wang P, Shen M, Zhou H, Meng C, Yuan A. MOF-Derived CuS@Cu-BTC Composites as High-Performance Anodes for Lithium-Ion Batteries. Small. 2019;15:1903522.

[5] Zhou H, Dai C, Liu Y, Fu X, Du Y. Experimental investigation of battery thermal management and safety with heat pipe and immersion phase change liquid. J Power Sources. 2020;473:228545.

[6] Wang F, Cao J, Ling Z, Zhang Z, Fang X. Experimental and simulative investigations on a phase change material nano-emulsion-based liquid cooling thermal management system for a lithium-ion battery pack. Energy. 2020;207.
[7] Lai Y, Wu W, Chen K, Wang S, Xin C. A compact and lightweight liquid-cooled thermal management solution for cylindrical lithium-ion power battery pack. Int J Heat Mass Transf. 2019;144:118581.
[8] Xu X, Li W, Xu B, Qin J. Numerical study on a water cooling system for prismatic LiFePO4 batteries at abused operating conditions. Appl Energy. 2019;250:404-12.
[9] Hamut HS, Dincer I, Naterer GF. Exergy analysis of a TMS (thermal management system) for range-extended EVs (electric vehicles). Energy. 2012;46:117-25.
[10] Jiang L, Zhang H, Li J, Xia P. Thermal performance of a cylindrical battery module impregnated with PCM composite based on thermoelectric cooling. Energy. 2019;188.
[11] Al-Zareer M, Dincer I, Rosen MA. A novel phase change based cooling system for prismatic lithium ion batteries. Int J Refrig. 2018;86:203-17.
[12] Bai F, Chen M, Song W, Yu Q, Li Y, Feng Z, Ding Y. Investigation of thermal management for lithium-ion pouch battery module based on phase change slurry and mini channel cooling plate. Energy. 2019;167:561-74.
[13] Ma Y, Mou H, Zhao H. Cooling optimization strategy for lithium-ion batteries based on triple-step nonlinear method. Energy. 2020;201.
[14] Chung Y, Kim MS. Thermal analysis and pack level design of battery thermal management system with liquid cooling for electric vehicles. Energy Convers Manag. 2019;196:105-16.
[15] Wu W, Wang S, Wu W, Chen K, Hong S, Lai Y. A critical review of battery thermal performance and liquid based battery thermal management. Energy Convers Manag. 2019;182:262-81.
[16] Cao J, Luo M, Fang X, Ling Z, Zhang Z. Liquid cooling with phase change materials for cylindrical Li-ion batteries: An experimental and numerical study. Energy. 2020;191.
[17] Xu X, Tong G, Li R. Numerical study and optimizing on cold plate splitter for lithium battery thermal management system. Appl Therm Eng. 2020;167:114787.
[18] Fang Y, Shen J, Zhu Y, Ye F, Li K, Su L. Investigation on the Transient Thermal Performance of a Mini-Channel Cold Plate for Battery Thermal Management. J Therm Sci. 2020.
[19] Chen K, Chen Y, Song M, Wang S. Multi-parameter structure design of parallel mini-channel cold plate for battery thermal management. Int J Energy Res. 2020;44:4321-34.
[20] Jarrett A, Kim IY. Design optimization of electric vehicle battery cooling plates for thermal performance. J Power Sources. 2011;196:10359-68.
[21] Deng T, Zhang G, Ran Y. Study on thermal management of rectangular Li-ion battery with serpentine-channel cold plate. Int J Heat Mass Transf. 2018;125:143-52.
[22] Sheng L, Su L, Zhang H, Li K, Fang Y, Ye W, Fang Y. Numerical investigation on a lithium ion battery thermal management utilizing a serpentine-channel liquid cooling plate exchanger. Int J Heat Mass Transf. 2019;141:658-68.
[23] E J, Han D, Qiu A, Zhu H, Deng Y, Chen J, Zhao X, Zuo W, Wang H, Chen J, Peng Q. Orthogonal experimental design of liquid-cooling structure on the cooling effect of a liquid-cooled battery thermal management system. Appl Therm Eng. 2018;132:508-20.
[24] Huo Y, Rao Z, Liu X, Zhao J. Investigation of power battery thermal management by using mini-channel cold plate. Energy Convers Manag. 2015;89:387-95.
[25] Qian Z, Li Y, Rao Z. Thermal performance of lithium-ion battery thermal management system by using mini-channel cooling. Energy Convers Manag. 2016;126:622-31.

[26] Rao Z, Zhang X. Investigation on thermal management performance of wedge-shaped microchannels for rectangular Li-ion batteries. Int J Energy Res. 2019;43:3876-90.
[27] Huang Y, Mei P, Lu Y, Huang R, Yu X, Chen Z, Roskilly AP. A novel approach for Lithium-ion battery thermal management with streamline shape mini channel cooling plates. Appl Therm Eng. 2019;157:113623.